Molecular MRI differentiation between primary central nervous system lymphomas and high-grade gliomas using endogenous protein-based amide proton transfer MR imaging at 3 Tesla

Shanshan Jiang,

Department of Radiology, Zhujiang Hospital, Southern Medical University, 253 Middle Gongye Road, Guangzhou, Guangdong 510282, China

Department of Radiology, Johns Hopkins University School of Medicine, 600 N. Wolfe Street, Baltimore, Maryland 21287, USA

Hao Yu,

Department of Radiology, Zhujiang Hospital, Southern Medical University, 253 Middle Gongye Road, Guangzhou, Guangdong 510282, China

Xianlong Wang,

Department of Radiology, Zhujiang Hospital, Southern Medical University, 253 Middle Gongye Road, Guangzhou, Guangdong 510282, China

Shilong Lu,

Department of Radiology, Zhujiang Hospital, Southern Medical University, 253 Middle Gongye Road, Guangzhou, Guangdong 510282, China

Yufa Li,

Department of Pathology, Zhujiang Hospital, Southern Medical University, 253 Middle Gongye Road, Guangzhou, Guangdong 510282, China

Lyujin Feng,

Department of Radiology, Zhujiang Hospital, Southern Medical University, 253 Middle Gongye Road, Guangzhou, Guangdong 510282, China

Yi Zhang,

Department of Radiology, Johns Hopkins University School of Medicine, 600 N. Wolfe Street, Baltimore, Maryland 21287, USA

Hye-Young Heo,

Department of Radiology, Johns Hopkins University School of Medicine, 600 N. Wolfe Street, Baltimore, Maryland 21287, USA

Dong-Hoon Lee,

Department of Radiology, Johns Hopkins University School of Medicine, 600 N. Wolfe Street, Baltimore, Maryland 21287, USA

Jinyuan Zhou, and

---

*Corresponding authors: Zhibo Wen, M.D., Ph.D., Phone: +86 20 6164 2782; zhibowen@163.com, or Jinyuan Zhou, Ph.D., Phone: +1 410 955 7491; Fax: +1 410 614 1977; jzhou@mri.jhu.edu.

Department of Radiology, Johns Hopkins University School of Medicine, 600 N. Wolfe Street, Baltimore, Maryland 21287, USA

Zhibo Wen

Department of Radiology, Zhujiang Hospital, Southern Medical University, 253 Middle Gongye Road, Guangzhou, Guangdong 510282, China

Abstract

Objectives—To show the ability of using the amide-proton-transfer-weighted (APTW) MRI signals as imaging biomarkers to differentiate primary central-nervous-system lymphomas (PCNSLs) from high-grade gliomas (HGGs).

Methods—Eleven patients with lymphomas and 21 patients with HGGs were examined. Magnetization-transfer (MT) spectra over an offset range of ± 6 ppm and the conventional MT ratio (MTR) at 15.6 ppm were acquired. The APTW signals, total chemical-exchange-saturation-transfer signal (integral between 0 and 5 ppm, $CEST_{total}$), and MTR signal were obtained and compared between PCNSLs and HGGs. The diagnostic performance was assessed with the receiver-operating-characteristic-curve analysis.

Results—The PCNSLs usually showed more homogeneous APTW hyperintensity (spatially compared to the normal brain tissue) than the HGGs. The $APTW_{max}$, $APTW_{max-min}$, and $CEST_{total}$ signal intensities were significantly lower ($P < 0.05$, 0.001, and 0.05, respectively), while the $APTW_{min}$ and MTR were significantly higher (both $P < 0.01$) in PCNSL lesions than in HGG lesions. The APTW values in peritumoral oedema were significantly lower for PCNSLs than for HGGs ($P < 0.01$). $APTW_{max-min}$ had the highest area under the receiver-operating-characteristic curve (0.963) and accuracy (94.1%) in differentiating PCNSLs from HGGs.

Conclusions—The protein-based APTW signal would be a valuable MRI biomarker by which to identify PCNSLs and HGGs presurgically.

Keywords

Introduction

Primary central nervous system cerebral lymphoma (PCNSL) causes approximately 5% of all primary brain tumours. Although a relatively lower incidence is found for PCNSL than for glioma, the most common malignant brain tumour, the incidence has increased drastically in both immunosuppressed and immunocompetent patients in recent decades [1, 2]. PCNSLs are usually treated by chemotherapy and whole-brain radiotherapy, while, with high-grade gliomas (HGGs), the treatment preference is a maximal safe resection, followed by chemotherapy and radiotherapy. Therefore, the precise preoperative differentiation of PCNSLs and HGGs is of significant practical relevance.

Brain MRI is a standard modality for imaging brain tumours in the clinic [3, 4]. However, there is a substantial overlap in the imaging features of PCNSLs and HGGs, both of which usually demonstrate gadolinium (Gd)-enhancing masses and surrounding oedema on

traditional MR images [5–7]. In recent years, it has been reported that several functional imaging parameters, using more advanced imaging techniques, may improve the discrimination of PCNSLs and HGGs, such as the apparent diffusion coefficient derived from diffusion imaging [8–12], tumour blood volume from the dynamic susceptibility contrast perfusion imaging [8, 10, 12, 13] or intravoxel incoherent motion imaging [10], intratumoral susceptibility signals on susceptibility-weighted imaging [14], and tumour blood flow from arterial spin labelling perfusion imaging [11, 15]. Although the results are promising, the sensitivity and specificity levels, and optimal cut-off values in differentiating these two tumours reported to date have been quite variable [8–15]. Currently, none of these modalities has been accepted as a gold standard for differential imaging diagnosis in the clinic.

Amide proton transfer (APT) imaging [16, 17] is a novel chemical exchange saturation transfer (CEST)-based molecular MRI technique [18–20] that detects endogenous mobile proteins and peptides in tissue, such as those dissolved in the cytoplasm. Note that semi-solid macromolecules in the more solid environment of the cell, such as those in the nucleus and the membrane, detectable by conventional magnetization transfer (MT) imaging (quantified by the MT ratio or MTR) [21], cannot be detected by APT imaging. The significance of using APT imaging is that the MRI contrast at the cellular protein level is achieved indirectly through the bulk water signal used in daily imaging. Many encouraging results have been reported by different research groups, regarding promising APT-weighted (APTW) signals as image biomarkers for brain tumours [22–27] and other cancers in the prostate, breast, and neck [28–31], and for cerebral ischemia [32–34], Parkinson's disease [35], and ventral hernia [36]. To the best of our knowledge, PCNSLs have never been studied with APT imaging, and the APT-MRI parameters have also not been quantitatively compared between PCNSLs and HGGs.

In this study, we assessed the diagnostic performance of APT imaging in the differentiation of PCNSLs and HGGs, and compared the results with semi-solid MT imaging. Previous pathologic reports revealed that the tumour cells of PCNSL had a high nuclear-cytoplasm (N/C) ratio and prominent nucleoli [37–39], and thus, a relatively low concentration of mobile proteins and peptides per unit tissue volume. Here, we hypothesize that the high N/C ratio and prominent nucleoli in the cells of PCNSL are associated with a relatively low APT-MRI signal and a relatively high MTR signal, compared with those of HGGs. We aimed to explore a non-invasive way of identifying PCNSLs and HGGs at the molecular level based on their APT-MRI signals.

Materials and methods

Subjects

This study was approved by the local Institutional Review Board, and all subjects gave written, informed consent prior to participation in this study. Between May 2011 and July 2014, potentially eligible patients were identified on the basis of the diagnosis of PCNSLs or HGGs. Only previously untreated candidates were enrolled (excluding patients who obtained treatments, such as corticosteroid administration, operation, chemotherapy, or radiotherapy), and none of the enrolled patients had neurologic disorders other than a

primary neoplasm. Thus, eleven PCNSL patients (six females, five males; mean age, 55.3 ± 13.7 years; age range, 36–79 years) with 13 lesions (one patient had three separate cerebral lesions) and 21 HGG patients (14 females, seven males; mean age, 45.0 ± 14.6 years; age range, 22–66 years) were included in the present study. All PCNSLs and HGGs were histopathologically diagnosed, and all PCNSLs were diffuse large B-cell lymphomas. Glioma grade was determined based on the 2007 WHO criteria.

MRI protocol

All patients were scanned on a Philips 3 T MRI system (Achieva 3.0 T; Philips Medical Systems, Best, The Netherlands) using a body coil for radiofrequency transmission and an eight-channel sensitivity encoding coil for reception. The routine MRI sequences performed for each patient included (field of view, 240×240 mm^2; matrix, 512×512; slice thickness, 6 mm): T_1-weighted (T_1W), T_2-weighted (T_2W), fluid-attenuated inversion recovery (FLAIR), APT imaging, and gadolinium contrast-enhanced T_1-weighted (Gd-T_1W). Gadopentetate dimeglumine (0.2 mL/kg body weight; Magnevist; Bayer Schering, Guangzhou, China) was finally injected to acquire Gd-T_1W images.

APT imaging was obtained using a fat-suppressed, fast spin-echo pulse sequence, with a pulse-train radiofrequency saturation (duration = 200 ms × 4; inter-pulse delay, 10 ms; power level = 2 μT) [22, 35]. The imaging parameters used were as follows: repetition time = 3 s; echo time = 11 ms; sensitivity-encoding factor = 2; matrix = 128 × 64 (reconstructed to be 400 × 400); field of view = 240 × 240 mm^2; and slice thickness = 6 mm. A multi-offset, multi-acquisition APT imaging acquisition protocol [31 offsets = 0, ± 0.25, ± 0.5, ± 0.75, ± 1, ± 1.5, ± 2, ± 2.5, ± 3 (2), ± 3.25 (4), ± 3.5 (8), ± 3.75 (4), ± 4 (2), ± 4.5, ± 5, ± 6 ppm; the values in parentheses were the number of acquisitions, which was 1, if not specified] was used. The higher number of acquisitions between ± 3 and ± 4 ppm were used to increase the signal-to-noise ratio of the APTW images. In addition, a saturated image at the offset of 15.6 ppm (2 kHz) was acquired to calculate the conventional MTR value with respect to the semi-solid MT imaging, and an unsaturated image was acquired for the signal normalization. APT scans were acquired at one FLAIR image slice showing the maximum tumour area, which was based on a qualitative analysis by visual inspection by a radiologist on site. The imaging time was about 3 min.

Image analysis

All raw image data were processed using the Interactive Data Language (IDL; ITT Visual Information Solutions, Boulder, CO, USA). The MT-spectrum (the normalized saturated imaging signal intensities as a function of frequency offsets, relative to the water resonance) was organized and corrected for the B_0 field heterogeneity effect on a voxel-by-voxel basis, as reported in the literature [22]. APT imaging was quantified through the MTR asymmetry analysis with respect to the water resonance. The calculated MTR$_{asym}$(3.5 ppm) image, using the B_0-corrected MT-spectrum data at the offset of ±3.5 ppm, was usually called the APTW image (Supplementary Information) [40]. The total CEST signal intensity (CEST$_{total}$) was defined as the integral of the whole MTR$_{asym}$ spectrum between 0 and 5 ppm (Supplementary Fig. S1). The different acquisition numbers at different frequency

offsets should not cause any problem for $CEST_{total}$, which depends on image intensities, not on noises.

Regions of interest (ROIs) were carefully chosen by two experienced radiologists (S.J. and X.W., who had nine and six years of experience in brain imaging, respectively). For each patient, similar to some previous reports [12, 25, 41], five ROIs were defined in the Gd-enhancing lesion area on the same Gd-T_1W image slice as APT imaging (Fig. 1). The peritumoral oedema (if present) and contralateral normal-appearing white matter (CNAWM) were also analyzed. No ROIs included areas of large liquefactive necrosis, haemorrhages, or large vessels evident on standard MRI sequences. The APTW signal intensity, MTR_{asym} spectrum, and MTR value were recorded for each ROI. The maximum APTW intensity ($APTW_{max}$), the minimum APTW intensity ($APTW_{min}$), the APTW signal heterogeneity within tumour cores ($APTW_{max-min} = APTW_{max} - APTW_{min}$), and the mean APTW intensity over all tumour ROIs ($APTW_{mean}$), the $CEST_{total}$ intensity (corresponding to the $APTW_{max}$), and the MTR value (corresponding to the $APTW_{max}$) from the lesions, as well as the APTW and the MTR values from the peritumoral oedema, were used to compare the two groups.

Histological data acquisition

One neuropathologist, blinded to the MRI features, reviewed histological samples from nine patients with PCNSL lesions and all 21 patients with HGG lesions. The histological data for the two remaining patients with PCNSL were kept at another institution and were not available for this study. Haematoxylin and eosin-stained (H&E) sections of 5-μm-thick formalin-fixed, paraffin-embedded tissue were examined.

The digital images captured using a microscope and a digital camera were analyzed with image analysis software (Image-Pro Plus, version 6.0, Media Cybernetics, Silver Spring, MD) by focusing on colour-specific features (blue-staining nuclei and pink-staining cytoplasm). One 0.044-mm^2 area of tissue was analyzed for each case. The field to capture was selected in areas of solid tumour with highest cell density and with the least amount of non-neoplastic tissue, such as blood vessels, major necrotic tissue, inflammatory cells, and tissue-sectioning artefacts. Furthermore, areas of the brain with single-cell tumour infiltration or reactive gliosis were avoided. The N/C ratio was calculated by dividing the nuclear area by the cytoplasmic area.

Statistical analysis

The interrater agreement between the two readers for the assessment of PCNSL and HHG was analyzed by using the Intraclass Correlation Coefficient (ICC) with 95% confidence intervals and by applying a one-way intraclass correlation coefficient with a random rater assumption. The comparisons of MRI parameters between the PCNSL and HGG groups were performed using an independent samples t-test to analyze the statistical differences. The sensitivity, specificity, and accuracy for the discrimination of PCNSLs and HHGs were calculated for the image parameters that showed significant statistical differences on the previous t-test, and the corresponding optimal cut-off values were determined by a receiver operator characteristics (ROC) analysis. Statistical analyses were performed using the

Statistical Package for the Social Sciences (SPSS, Version 19.0; Chicago, Illinois, USA). The alpha level of all tests was set at $P < 0.05$.

Results

Comparison of APTW image features

We first assessed the radiographic features of the PCNSLs and the HGGs, using several standard (T_1W, T_2W, Gd-T_1W, MTR) and APTW sequences. Fig. 2 shows one example of these standard and APTW MR images for a PCNSL patient, as well as high-power photomicrographs of the corresponding H&E-stained sections. For the PCNSLs, a total of 13 lesions were observed in 11 PCNSL patients scanned, nine of which were located in the cerebral deep white matter, one in the surface of the cerebral hemisphere, two with the major lesion in the ventricle (one lesion showed no visible peritumoral oedema), and one in the cerebellar hemisphere. These lesions showed homogeneous ($n = 9$) or to some extent heterogeneous, either fissuring necrotic ($n = 3$) or central faint ($n = 1$), Gd enhancements on the post-contrast T_1W images. The APTW images overall showed visually homogenous APTW hyperintensities (spatially compared to the CNAWM) in the Gd-enhancing areas on the Gd-T_1W images. The lesions identified by APTW were smaller than or approximately equal to those identified by T_1W, T_2W, and MTR, but were almost equal to the lesions identified on the Gd-T_1W images.

Fig. 3 shows standard and APTW MR images for two HGG patients, as well as high-power photomicrographs of the corresponding H&E-stained sections. All 21 HGG lesions (glioblastoma, $n = 15$; anaplastic oligodendroglioma, $n = 2$; anaplastic astrocytomas, $n = 4$), located in the cerebral parenchyma ($n = 19$), the cerebellar hemisphere ($n = 1$), or the ventricle ($n = 1$), showed considerable heterogeneous Gd enhancements (except for one case in Fig. 3b, showing slightly Gd-enhancing) on the post-contrast T_1W images, and three lesions showed no visible peritumoral oedema. Notably, the APTW images demonstrated quite heterogeneous APTW hyperintensities (compared to the CNAWM) in the Gd-enhancing areas on the Gd-T_1W images, showing the HGG lesions as ring-like ($n = 10$), nodular ($n = 5$), or patchy ($n = 6$) heterogeneous masses. The lesions identified by APTW were smaller than or approximately equal to those identified by T_1W, T_2W, and MTR, but larger than or approximately equal to those identified by Gd-T_1W.

Quantitative image analysis

Interrater reliability, as determined by ICC, was acceptable for both PCNLs and HHGs, and there was a good consistency between raters with the ICC values of tumour $APTW_{max}$, $APTW_{min}$, $APTW_{max-min}$, $APTW_{mean}$, $CEST_{total,}$ and MTR values of 0.982, 0.939, 0.965, 0.984, 0.951, and 0.869, respectively.

For the PCNSL and HGG lesions encircled by the Gd enhancement (Fig. 4a and b), the PCNSLs had significantly lower $APTW_{max}$ ($3.38\% \pm 1.06\%$), $APTW_{max-min}$ ($0.76\% \pm 0.42\%$), and $CEST_{total}$ ($11.22\% \pm 3.47\%$) values than the HGGs ($APTW_{max} = 4.36\% \pm 1.30\%$, $P < 0.05$; $APTW_{max-min} = 2.55\% \pm 1.20\%$, $P < 0.01$; $CEST_{total} = 14.34\% \pm 4.04\%$, $P < 0.05$), and a significantly higher $APTW_{min}$ ($2.62\% \pm 0.90\%$) value than the HGGs

(APTW$_{min}$ = 1.81% ± 0.65%, P < 0.01). It is interesting that the APTW$_{mean}$ showed no statistical difference between the PCNSLs (3.01% ± 0.98%) and the HGGs (3.06% ± 0.81%, P = 0.879). On the contrary, the MTR value for the PCNSLs (19.22% ± 3.36%) was significantly higher than that for the HGGs (13.43% ± 5.40%, P < 0.01).

When the peritumoral oedema areas were compared (Fig. 4c and d), the oedema APTW values were significantly lower for the PCNSLs (1.66% ± 0.61%) than for the HGGs (2.45% ± 0.83%, P < 0.01), but the oedema MTR values showed no statistical difference between the PCNSLs (22.20% ± 4.86%) and the HGGs (18.77% ± 4.11%, P = 0.058).

The results of the ROC analysis are summarized in Table 1. The areas under the curve (AUCs) were: 0.707 for tumour APTW$_{max}$; 0.751 for tumour APTW$_{min}$; 0.963 for tumour APTW$_{max-min}$; 0.733 for tumour CEST$_{total}$; 0.828 for tumour MTR; and 0.755 for oedema APTW. Tumour APTW heterogeneity (APTW$_{max-min}$) had the highest AUC and accuracy (94.1%) in differentiating PCNSLs from HGGs.

Discussion

In this study, we assessed the diagnostic performance of APT imaging and MT imaging to facilitate the preoperative differentiation of PCNSLs and HGGs. Our principal findings can be summarized as follows. (i) The PCNSL lesions encircled by the Gd enhancement usually demonstrated relatively homogeneous hyperintensity (spatially compared to the CNAWM), while the HGG lesions usually showed heterogeneous hyperintensity on the APTW images (Figs. 2 and 3). (ii) Quantitative image analysis showed that the PCNSL lesions demonstrated significantly lower APTW$_{max}$, APTW$_{max-min}$, and CEST$_{total}$ (corresponding to the APTW$_{max}$) signals and a significantly higher APTW$_{min}$ signal than the HGG lesions (Fig. 4). In addition, the mean MTR value in the PCNSL lesions (corresponding to the APTW$_{max}$) was significantly higher than that in the HGG lesions. (iii) The APTW values in peritumoral oedema were significantly higher for HGGs than for PCNSLs (Fig. 4), which may represent HGG tumour cell infiltration.

Technically, APT imaging was designed to detect mobile proteins and peptides in tissue [42], while conventional MT imaging is sensitive to semi-solid macromolecules in the more solid environment of the cell [21]. In this study, the APTW signals (APTW$_{max}$, APTW$_{min}$, APTW$_{max-min}$, and APTW$_{mean}$), the CEST$_{total}$ signal, and the MTR signal were compared in two different tumour lesions. It is well known [37–39] that the PCNSL lesions are associated with a higher N/C ratio, demonstrating less cytoplasm volume accompanied by more nuclei and membranes, compared with the HGG lesions. The significantly lower APTW$_{max}$ and CEST$_{total}$ values and significantly higher MTR value in the PCNSL group than in the HGG group were consistent with the histological characteristics of higher N/C ratios in PCNSLs, as reported in the literature [37–39], and also verified the contrast mechanisms of APT and MTR imaging. Furthermore, the APTW$_{max-min}$ parameter indicated the APTW signal heterogeneity within the lesion. Unlike the HGGs, most PCNSLs, especially those in the immunocompetent patients, are histologically relatively homogenous [43, 44]. In this study, we found that the PCNSLs showed significantly lower APTW$_{max-min}$ than the HGGs, quite consistent with the histopathological features of the PCNSLs.

The preoperative differentiation of PCNSLs and HGGs is not always feasible with conventional or advanced MRI sequences, particularly for atypical lymphomas presenting heterogeneous contrast enhancement or for atypical glioblastomas presenting homogenous contrast enhancement (Fig. 3b). For 32 participants in this study, the sensitivity and specificity for differentiating HGGs from PCNSLs were, respectively, 100% and 36.4% (by a junior radiologist, L.F., with two years of experience in brain imaging, blinded to the pathology reports, based on several conventional MRI sequences, T_2W, FLAIR, T_1W, and Gd-T_1W, acquired on the same day as APT), or 100% and 72.7% (according to official radiology reports, performed typically by experienced neuroradiologists, based on all available conventional and advanced MRI sequences, acquired on the same day or on several different days). It is generally believed that protein-based APT imaging would be more specific than conventional water-based MRI for brain tumours. Several previous studies [22–27] have demonstrated that the APT technique has the potential to separate high- from low-grade gliomas, the potential to differentiate between tumour and peritumoral oedema, and the potential to differentiate between tumour recurrence and treatment effects. Our early results in this study have shown that the APTW MRI signal is a valuable imaging biomarker for the differential diagnosis of HGGs and PCNSLs. Currently, APT imaging is still in its infancy. The maximal APT signal in the tumour could be 3–5% of the bulk water intensity (Fig. 4). Thus, APT imaging should have higher signal-to-noise ratios than some blood flow and blood volume imaging techniques, such as the arterial spin labelling imaging (about 1–2% of the bulk water intensity) [11, 15]. Notably, one can expect that the use of a fast three-dimensional APT imaging sequence that has recently become available on clinical 3 T MRI scanners [24] would further improve the accuracy of future APTW measurements. Furthermore, it was reported that roughly 10% of glioblastomas and 30% of anaplastic astrocytoma demonstrate no Gd enhancement [45]. Therefore, additional MR approaches, especially those based on endogenous contrast agents, like APT imaging, are much needed. Notably, it has been shown that APTW hyperintensity is a typical feature of HGGs, independent of Gd enhancement [24]. This is particularly significant for patients with non-enhancing high-grade lesions, and for those with a contraindication to Gd administration. Therefore, the endogenous protein-based APTW image features would be a very useful MRI biomarker for assessing PCNSLs versus HGGs non-invasively and reliably.

There are some limitations or weaknesses in this study. (i) The sample size of PCNSLs was small because of the rare incidence of these tumours, and all PCNSL cases recruited in this study were immunocompetent patients. Thus, it may be difficult to determine any true optimal threshold values from this dataset. A large-scale study including both immunosuppressed and immunocompetent patients would be required to obtain more conclusive results. (ii) The APT experiment covered only one slice. Thus, the MRI signal changes in other brain regions could not be evaluated in the present study. The voxel size of the APT experiment was $1.88 \times 3.75 \times 6$ mm, which was relatively large (due to the small APT effect). This would potentially lead to homogeneous APTW hyperintensities due to the large partial volume effect. (iii) No exact correspondence between pathologic specimens and the MRI sequences was obtained in this study. Therefore, the relationships between the APTW or MTR signals and N/C ratios could not be assessed quantitatively.

In conclusion, the present study represents the first analysis of the ability to use APT MRI to differentiate between PCNSLs and HGGs. The data showed that lower $APTW_{max}$, $APTW_{max-min}$, and $CEST_{total}$, and higher $APTW_{min}$ and MTR are most likely be associated with a PCNSL, whereas higher $APTW_{max}$, $APTW_{max-min}$, and $CEST_{total}$ and lower $APTW_{min}$ and MTR are most likely associated with an HGG. $APTW_{max-min}$ had the highest AUC and accuracy, and outperformed all other parameters in separating PCNSLs from HGGs. Our early results suggest that the endogenous protein-based APTW signal may be a valuable MRI biomarker by which to identify PCNSLs and HGGs presurgically. APT-MRI is a safe, completely non-invasive technology, and the results can be readily translated into the clinic. The addition of APT imaging to the currently used MRI protocol (including the conventional and advanced MRI sequences) would greatly enhance the diagnostic accuracy of MRI for these brain malignancies ultimately.

Supplementary Material

Refer to Web version on PubMed Central for supplementary material.

Acknowledgment

Abbreviations

APT	amide proton transfer
APTW	amide proton transfer-weighted
CEST	chemical exchange saturation transfer
CNAWM	contralateral normal-appearing white matter
Gd	gadolinium
H&E	haematoxylin and eosin-stained
HGG	high-grade glioma
MT	magnetization transfer
MTR$_{asym}$	magnetization transfer-ratio asymmetry
N/C	nuclear-cytoplasm
PCNSL	primary central nervous system cerebral lymphoma
ROC	receiver operator characteristics
ROI	region of interest
T$_1$W	T$_1$-weighted

T2W T_2-weighted

FLAIR   fluid-attenuated inversion recovery

References

1. Corn BW, Marcus SM, Topham A, Hauck W, Curran WJ Jr. Will primary central nervous system lymphoma be the most frequent brain tumor diagnosed in the year 2000? Cancer. 1997; 79:2409–2413. [PubMed: 9191531]

2. DeAngelis LM, Seiferheld W, Schold SC, Fisher B, Schultz CJ. Combination chemotherapy and radiotherapy for primary central nervous system lymphoma: Radiation Therapy Oncology Group study 93-10. J Clin Oncol. 2002; 20:4643–4648. [PubMed: 12488408]

3. Wen PY, Macdonald DR, Reardon DA, et al. Updated response assessment criteria for high-grade gliomas: response assessment in neuro-oncology working group. J Clin Oncol. 2010; 28:1963–1972. [PubMed: 20231676]

4. Hu LS, Eschbacher JM, Heiserman JE, et al. Reevaluating the imaging definition of tumor progression: perfusion MRI quantifies recurrent glioblastoma tumor fraction, pseudoprogression, and radiation necrosis to predict survival. Neuro-Oncology. 2012; 14:919–930. [PubMed: 22561797]

5. Go JL, Lee SC, Kim PE. Imaging of primary central nervous system lymphoma. Neurosurg Focus. 2006; 21:E4. [PubMed: 17134120]

6. Lolli V, Tampieri D, Melancon D, Delpilar Cortes M. Imaging in primary central nervous system lymphoma. Neuroradiol J. 2010; 23:680–689. [PubMed: 24148721]

7. Tang YZ, Booth TC, Bhogal P, Malhotra A, Wilhelm T. Imaging of primary central nervous system lymphoma. Clin Radiol. 2011; 66:768–777. [PubMed: 21513925]

8. Wang S, Kim S, Chawla S, et al. Differentiation between glioblastomas, solitary brain metastases, and primary cerebral lymphomas using diffusion tensor and dynamic susceptibility contrast-enhanced MR imaging. AJNR Am J Neuroradiol. 2011; 32:507–514. [PubMed: 21330399]

9. Doskaliyev A, Yamasaki F, Ohtaki M, et al. Lymphomas and glioblastomas: differences in the apparent diffusion coefficient evaluated with high b-value diffusion-weighted magnetic resonance imaging at 3T. Eur J Radiol. 2012; 81:339–344. [PubMed: 21129872]

10. Suh CH, Kim HS, Lee SS, et al. Atypical imaging features of primary central nervous system lymphoma that mimics glioblastoma: utility of intravoxel incoherent motion MR imaging. Radiology. 2014; 272:504–513. [PubMed: 24697149]

11. Yamashita K, Yoshiura T, Hiwatashi A, et al. Differentiating primary CNS lymphoma from glioblastoma multiforme: assessment using arterial spin labeling, diffusion-weighted imaging, and (1)(8)F-fluorodeoxyglucose positron emission tomography. Neuroradiology. 2013; 55:135–143. [PubMed: 22961074]

12. Kickingereder P, Wiestler B, Sahm F, et al. Primary central nervous system lymphoma and atypical glioblastoma: multiparametric differentiation by using diffusion-, perfusion-, and susceptibility-weighted MR imaging. Radiology. 2014; 272:843–850. [PubMed: 24814181]

13. Toh CH, Wei KC, Chang CN, Ng SH, Wong HF. Differentiation of primary central nervous system lymphomas and glioblastomas: comparisons of diagnostic performance of dynamic susceptibility contrast-enhanced perfusion MR imaging without and with contrast-leakage correction. AJNR Am J Neuroradiol. 2013; 34:1145–1149. [PubMed: 23348763]

14. Peters S, Knoss N, Wodarg F, Cnyrim C, Jansen O. Glioblastomas vs. lymphomas: more diagnostic certainty by using susceptibility-weighted imaging (SWI). Rofo. 2012; 184:713–718. [PubMed: 22618484]

15. Furtner J, Schopf V, Preusser M, et al. Non-invasive assessment of intratumoral vascularity using arterial spin labeling: A comparison to susceptibility-weighted imaging for the differentiation of primary cerebral lymphoma and glioblastoma. Eur J Radiol. 2014; 83:806–810. [PubMed: 24613549]

16. Zhou J, Payen J, Wilson DA, Traystman RJ, van Zijl PCM. Using the amide proton signals of intracellular proteins and peptides to detect pH effects in MRI. Nature Med. 2003; 9:1085–1090. [PubMed: 12872167]

17. Zhou J, Lal B, Wilson DA, Laterra J, van Zijl PCM. Amide proton transfer (APT) contrast for imaging of brain tumors. Magn Reson Med. 2003; 50:1120–1126. [PubMed: 14648559]

18. Ward KM, Aletras AH, Balaban RS. A new class of contrast agents for MRI based on proton chemical exchange dependent saturation transfer (CEST). J Magn Reson. 2000; 143:79–87. [PubMed: 10698648]

19. Zhou J, van Zijl PC. Chemical exchange saturation transfer imaging and spectroscopy. Progr NMR Spectr. 2006; 48:109–136.

20. Zaiss M, Bachert P. Chemical exchange saturation transfer (CEST) and MR Z-spectroscopy in vivo: a review of theoretical approaches and methods. Phys Med Biol. 2013; 58:R221–R269. [PubMed: 24201125]

21. Henkelman RM, Stanisz GJ, Graham SJ. Magnetization transfer in MRI: a review. NMR Biomed. 2001; 14:57–64. [PubMed: 11320533]

22. Wen Z, Hu S, Huang F, et al. MR imaging of high-grade brain tumors using endogenous protein and peptide-based contrast. Neuroimage. 2010; 51:616–622. [PubMed: 20188197]

23. Zhou J, Tryggestad E, Wen Z, et al. Differentiation between glioma and radiation necrosis using molecular magnetic resonance imaging of endogenous proteins and peptides. Nature Med. 2011; 17:130–134. [PubMed: 21170048]

24. Zhou J, Zhu H, Lim M, et al. Three-dimensional amide proton transfer MR imaging of gliomas: Initial experience and comparison with gadolinium enhancement. J Magn Reson Imaging. 2013; 38:1119–1128. [PubMed: 23440878]

25. Togao O, Yoshiura T, Keupp J, et al. Amide proton transfer imaging of adult diffuse gliomas: correlation with histopathological grades. Neuro Oncol. 2014; 16:441–448. [PubMed: 24305718]

26. Hong X, Liu L, Wang M, et al. Quantitative multiparametric MRI assessment of glioma response to radiotherapy in a rat model. Neuro Oncol. 2014; 16:856–867. [PubMed: 24366911]

27. Sagiyama K, Mashimo T, Togao O, et al. In vivo chemical exchange saturation transfer imaging allows early detection of a therapeutic response in glioblastoma. Proc Natl Acad Sci (USA). 2014; 111:4542–4547. [PubMed: 24616497]

28. Jia G, Abaza R, Williams JD, et al. Amide proton transfer MR imaging of prostate cancer: A preliminary study. J Magn Reson Imaging. 2011; 33:647–654. [PubMed: 21563248]

29. Klomp DW, Dula AN, Arlinghaus LR, et al. Amide proton transfer imaging of the human breast at 7T: development and reproducibility. NMR Biomed. 2013; 26:1271–1277. [PubMed: 23559550]

30. Dula AN, Arlinghaus LR, Dortch RD, et al. Amide proton transfer imaging of the breast at 3 T: establishing reproducibility and possible feasibility assessing chemotherapy response. Magn Reson Med. 2013; 70:216–224. [PubMed: 22907893]

31. Yuan J, Chen S, King AD, et al. Amide proton transfer-weighted imaging of the head and neck at 3 T: a feasibility study on healthy human subjects and patients with head and neck cancer. NMR Biomed. 2014; 27:1239–1247. [PubMed: 25137521]

32. Zhao X, Wen Z, Huang F, et al. Saturation power dependence of amide proton transfer image contrasts in human brain tumors and strokes at 3 T. Magn Reson Med. 2011; 66:1033–1041. [PubMed: 21394783]

33. Tietze A, Blicher J, Mikkelsen IK, et al. Assessment of ischemic penumbra in patients with hyperacute stroke using amide proton transfer (APT) chemical exchange saturation transfer (CEST) MRI. NMR Biomed. 2014; 27:163–174. [PubMed: 24288260]

34. Tee YK, Harston GW, Blockley N, et al. Comparing different analysis methods for quantifying the MRI amide proton transfer (APT) effect in hyperacute stroke patients. NMR Biomed. 2014; 27:1019–1029. [PubMed: 24913989]

35. Li C, Peng S, Wang R, et al. Chemical exchange saturation transfer MR imaging of Parkinson's disease at 3 Tesla. Eur Radiol. 2014; 24:2631–2639. [PubMed: 25038850]

36. Franconi F, Roux J, Garric X, Lemaire L. Early postsurgical visualization of composite mesh used in ventral hernia repair by amide proton transfer MRI. Magn Reson Med. 2014; 71:313–317. [PubMed: 23423985]

37. Kalakunja A, Hardwicke F. Non-Hodgkin's lymphoma occurring as pure central nervous system pathology. Clin Adv Hematol Oncol. 2003; 1:554–555. [PubMed: 16258448]

38. Commins DL. Pathology of primary central nervous system lymphoma. Neurosurg Focus. 2006; 21:E2. [PubMed: 17134118]

39. Rubenstein J, Ferreri AJ, Pittaluga S. Primary lymphoma of the central nervous system: epidemiology, pathology and current approaches to diagnosis, prognosis and treatment. Leuk Lymphoma. 2008; 49:S43–S51.

40. Zhou J, Blakeley JO, Hua J, et al. Practical data acquisition method for human brain tumor amide proton transfer (APT) imaging. Magn Reson Med. 2008; 60:842–849. [PubMed: 18816868]

41. Murakami R, Hirai T, Sugahara T, et al. Grading astrocytic tumors by using apparent diffusion coefficient parameters: superiority of a one- versus two-parameter pilot method. Radiology. 2009; 251:838–845. [PubMed: 19318585]

42. Zhou J, Yan K, Zhu H. A simple model for understanding the origin of the amide proton transfer MRI signal in tissue. Appl Magn Reson. 2012; 42:393–402. [PubMed: 23243339]

43. Imai H, Shimada K, Shimada S, et al. Comparative clinicopathological study of primary CNS diffuse large B-cell lymphoma and intravascular large B-cell lymphoma. Pathol Int. 2009; 59:431–437. [PubMed: 19563405]

44. Preusser M, Woehrer A, Koperek O, et al. Primary central nervous system lymphoma: a clinicopathological study of 75 cases. Pathology. 2010; 42:547–552. [PubMed: 20854073]

45. Scott JN, Brasher PM, Sevick RJ, Rewcastle NB, Forsyth PA. How often are nonenhancing supratentorial gliomas malignant? A population study. Neurology. 2002; 59:947–949. [PubMed: 12297589]

Key Points

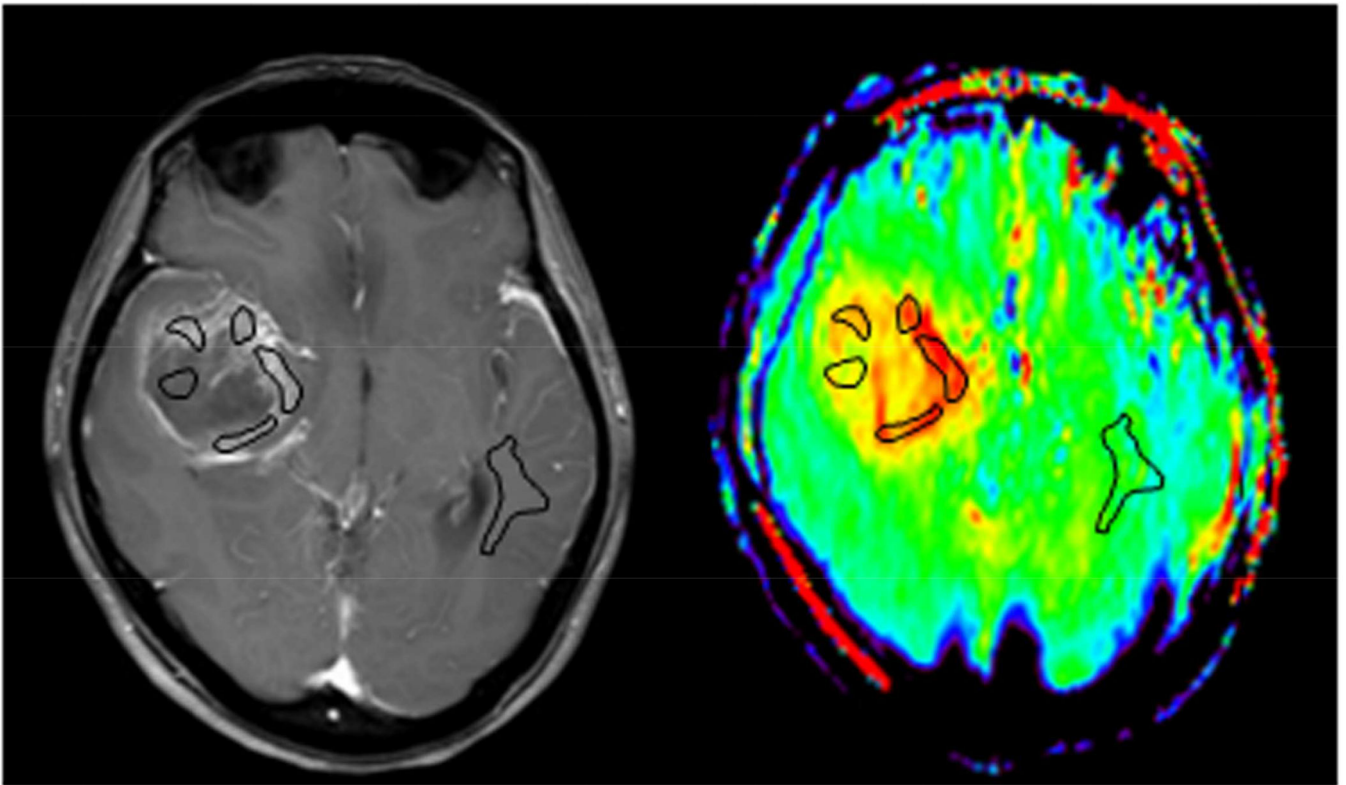PCNSLs overall showed more homogeneous APTW hyperintensity than HGGs.

Maximum APTW signals were lower in PCNSL lesions than in HGG lesions.

MTR signals were higher in PCNSLs than in HGGs.

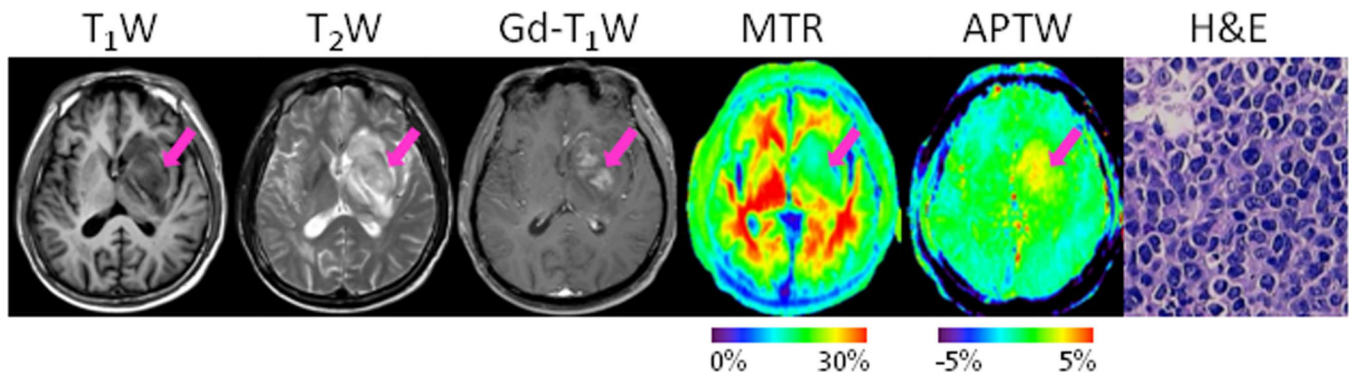APTW heterogeneity had the highest accuracy in differentiating PCNSLs from HGGs.

Fig. 1.
Example of the placement of ROIs. Five ROIs were placed in the tumour core encircled by the Gd enhancement, with reference to other traditional images, and one ROI was placed in the CNAWM.

Fig. 2.
Standard and APTW MR images, and high-power H&E-stained sections (original magnification, ×200) of a germinal centre B-cell-like, diffuse large B-cell lymphoma (pink arrows) in the left basal ganglion in a 60-year-old man. Gd-T_1W image demonstrated a flocculent Gd-enhancing tumour mass. MTR image showed that the entire tumour was hypointense. APTW image showed a relatively homogeneous tumour mass, with intermediate APTW signal intensities of 2.42%– 3.04% (compared to the CNAWM, 0.08%). H&E-stained section showed dense aggregate cells with high N/C ratio (2.43), scanty cytoplasm, and pleomorphic nuclei of variable size, shape, staining density, and nucleolar prominence.
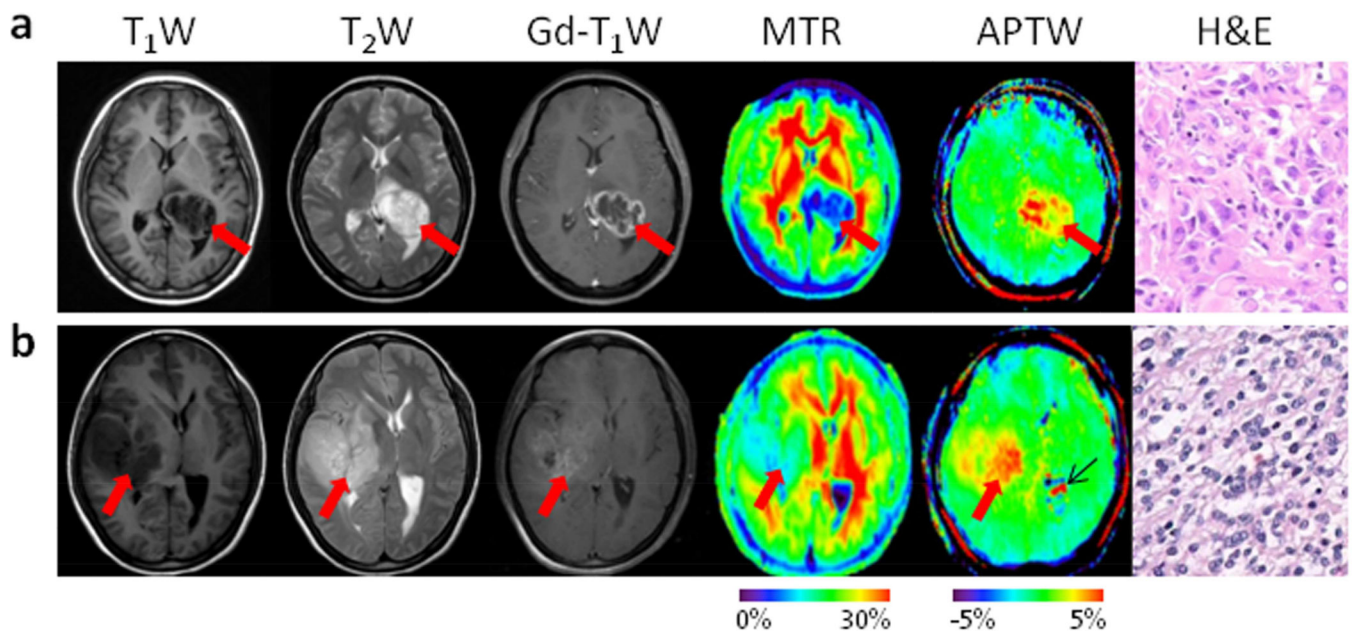
Fig. 3.
Standard and APTW MR images, and high-power H&E-stained sections (original magnification, ×200) of two pathologically confirmed HGGs. **a** A typical glioblastoma (red arrows) in the left ventricle in a 23-year-old woman. Gd-T_1W image demonstrated heterogeneous, irregular ring-like contrast enhancement (the typical imaging characteristics of a HGG). APTW image showed a heterogeneously hyperintense, ring-like tumour mass, with APTW signal intensities from 2.51%–6.84% (compared to the CNAWM, 0.76%). H&E-stained section showed many multinucleated, nuclear atypical tumour cells with more abundant cytoplasm. The N/C ratio was as low as 0.28. **b** An anaplastic oligodendroglioma (red arrows) in the right temporal lobe in a 37-year-old woman. Gd-T_1W image demonstrated a patchy, slightly Gd-enhancing tumour mass. APTW image showed a heterogeneously hyperintense, nodular tumour mass, with APTW signal intensities from 2.70%–4.04% (compared to the CNAWM, 0.44%). H&E-stained section showed numerous larger and richer nuclei in chromatin, accompanying with the atypical mitosis, and scanty eosinophilic fibrillary cytoplasm amidst a mucinous background. The N/C ratio was as low as 0.34. An eccentric calcification or remote haemorrhage (white arrow) was noted. The ventricle-related image artefact (black arrow) can also be seen.
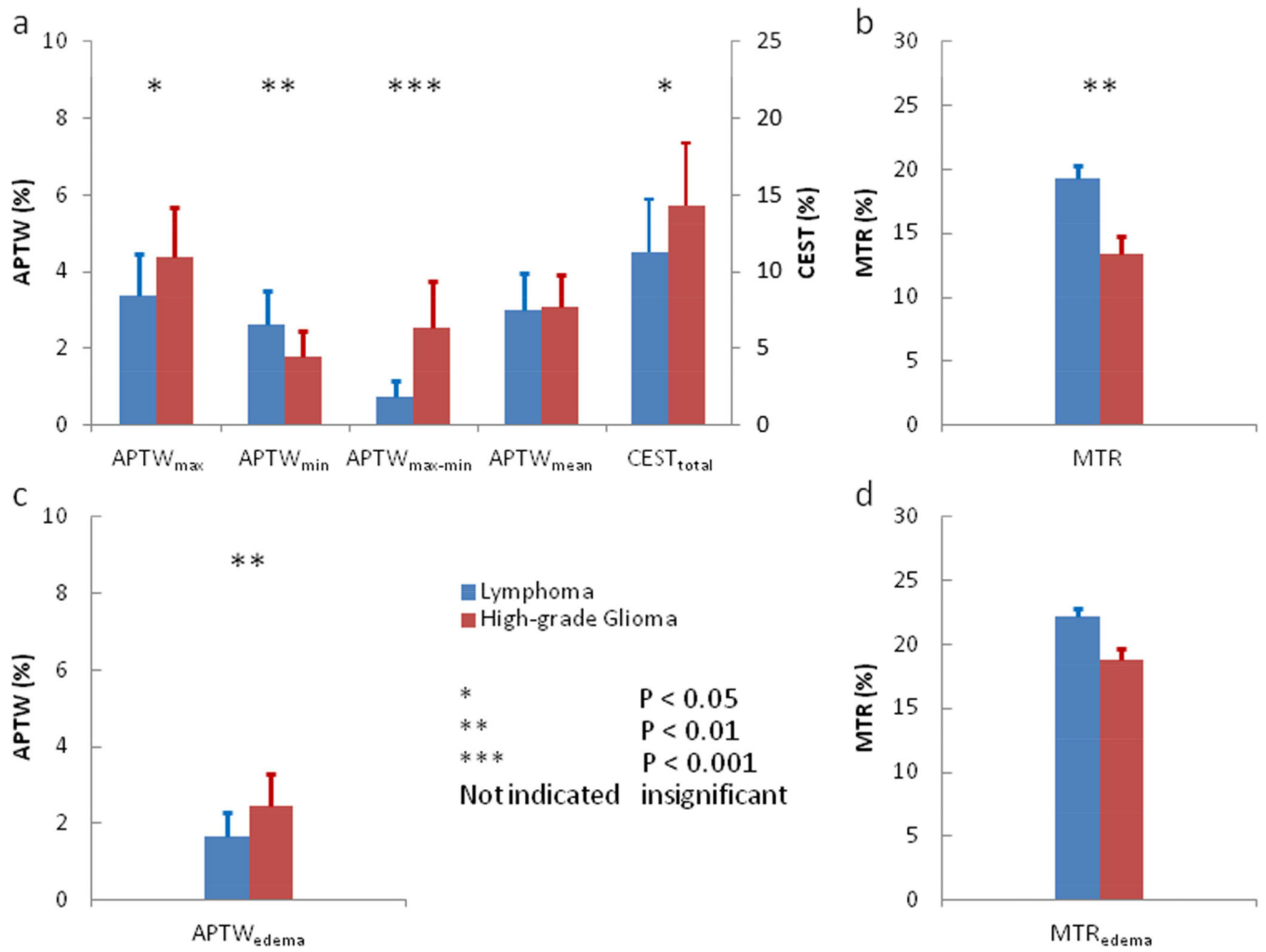
Fig. 4.

Comparisons of the APTW signal intensities (APTW$_{max}$, APTW$_{min}$, APTW$_{max-min}$, and APTW$_{mean}$) and the total CEST signal intensities (CEST$_{total}$) (**a**), as well as the MTR values (**b**) measured from the PCNSL and HGG lesions. Comparisons of the APTW (**c**) and the MTR (**d**) values measured in peritumoral oedema for PCNSLs and HGGs. CEST$_{total}$ included various CEST effects appearing at an offset range of 0–5 ppm. All parameters were quantified by % water signal intensity.

Table 1

ROC analysis results of tumor $APTW_{max}$, $APTW_{min}$, $APTW_{max-min}$, $CEST_{total}$, and MTR values and edema APTW values in differentiating HHGs (n = 21) from PCNSLs (n = 11)

Parameter	AUC	95% CI	P value	Cut-off	Sensitivity	Specificity	Accuracy
Tumor: $APTW_{max}$	0.707	0.518 – 0.896	0.045	3.13%	95.2%	53.8%	79.4%
$APTW_{min}$	0.751	0.566 – 0.936	0.015	2.47%	85.7%	61.5%	76.5%
$APTW_{max-min}$	0.963	0.901 – 1.000	0.000	1.14%	100%	84.6%	94.1%
$CEST_{total}$	0.733	0.555 – 0.910	0.024	10.69%	95.2%	53.8%	79.4%
MTR	0.828	0.687 – 0.969	0.002	15.6%	61.9%	92.3%	73.5%
Edema: APTW	0.755	0.578 – 0.931	0.020	1.56%	94.4%	50.0%	76.7%

When the ROC curve analysis was performed, the tumor $APTW_{min}$ and MTR values were processed, respectively, using (10% - $APTW_{min}$) and (100% - MTR) as new variables to maintain the same trend as the other parameters in differentiating PCNSLs from HGGs. AUC, area under the curve; CI, confidence interval